



**HAL**  
open science

## Submillimetre galaxies reside in dark matter haloes with masses greater than $3 \times 10^{11}$ solar masses

Alexandre Amblard, Asantha Cooray, Paolo Serra, B. Altieri, V. Arumugam, H. Aussel, A. Blain, J. Bock, A. Boselli, V. Buat, et al.

### ► To cite this version:

Alexandre Amblard, Asantha Cooray, Paolo Serra, B. Altieri, V. Arumugam, et al.. Submillimetre galaxies reside in dark matter haloes with masses greater than  $3 \times 10^{11}$  solar masses. *Nature*, 2011, 470 (7335), pp.510-512. 10.1038/nature09771 . cea-00904021

**HAL Id: cea-00904021**

**<https://cea.hal.science/cea-00904021>**

Submitted on 9 Feb 2021

**HAL** is a multi-disciplinary open access archive for the deposit and dissemination of scientific research documents, whether they are published or not. The documents may come from teaching and research institutions in France or abroad, or from public or private research centers.

L'archive ouverte pluridisciplinaire **HAL**, est destinée au dépôt et à la diffusion de documents scientifiques de niveau recherche, publiés ou non, émanant des établissements d'enseignement et de recherche français ou étrangers, des laboratoires publics ou privés.

# Sub-millimetre galaxies reside in dark matter halos with masses greater than $3 \times 10^{11} M_{\odot}$

A. Amblard<sup>1</sup>, A. Cooray<sup>1,2</sup>, P. Serra<sup>1</sup>, B. Altieri<sup>3</sup>, V. Arumugam<sup>4</sup>, H. Aussel<sup>5</sup>, A. Blain<sup>2</sup>, J. Bock<sup>2,6</sup>, A. Boselli<sup>7</sup>, V. Buat<sup>7</sup>, N. Castro-Rodríguez<sup>8,9</sup>, A. Cava<sup>8,9</sup>, P. Chanial<sup>10</sup>, E. Chapin<sup>11</sup>, D.L. Clements<sup>10</sup>, A. Conley<sup>12</sup>, L. Conversi<sup>3</sup>, C.D. Dowell<sup>2,6</sup>, E. Dwek<sup>13</sup>, S. Eales<sup>14</sup>, D. Elbaz<sup>5</sup>, D. Farrah<sup>15</sup>, A. Franceschini<sup>16</sup>, W. Gear<sup>14</sup>, J. Glenn<sup>12</sup>, M. Griffin<sup>14</sup>, M. Halpern<sup>11</sup>, E. Hatziminaoglou<sup>17</sup>, E. Ibar<sup>18</sup>, K. Isaak<sup>14</sup>, R.J. Ivison<sup>18,4</sup>, A.A. Khostovan<sup>1</sup>, G. Lagache<sup>19</sup>, L. Levenson<sup>2,6</sup>, N. Lu<sup>2,20</sup>, S. Madden<sup>5</sup>, B. Maffei<sup>21</sup>, G. Mainetti<sup>16</sup>, L. Marchetti<sup>16</sup>, G. Marsden<sup>11</sup>, K. Mitchell-Wynne<sup>1</sup>, H.T. Nguyen<sup>6,2</sup>, B. O'Halloran<sup>10</sup>, S.J. Oliver<sup>15</sup>, A. Omont<sup>22</sup>, M.J. Page<sup>23</sup>, P. Panuzzo<sup>5</sup>, A. Papageorgiou<sup>14</sup>, C.P. Pearson<sup>23,24</sup>, I. Pérez-Fournon<sup>8,9</sup>, M. Pohlen<sup>14</sup>, N. Rangwala<sup>12</sup>, I.G. Roseboom<sup>15</sup>, M. Rowan-Robinson<sup>10</sup>, M. Sánchez Portal<sup>3</sup>, B. Schulz<sup>2,20</sup>, Douglas Scott<sup>11</sup>, N. Seymour<sup>23</sup>, D.L. Shupe<sup>2,20</sup>, A.J. Smith<sup>15</sup>, J.A. Stevens<sup>25</sup>, M. Symeonidis<sup>23</sup>, M. Trichas<sup>10</sup>, K. Tugwell<sup>26</sup>, M. Vaccari<sup>16</sup>, E. Valiante<sup>11</sup>, I. Valtchanov<sup>3</sup>, J. D. Vieira<sup>2</sup>, L. Vigroux<sup>22</sup>, L. Wang<sup>15</sup>, R. Ward<sup>15</sup>, G. Wright<sup>18</sup>, C.K. Xu<sup>2,20</sup>, & M. Zemcov<sup>2,6</sup>

<sup>1</sup>*Dept. of Physics & Astronomy, University of California, Irvine, CA 92697, USA*

<sup>2</sup>*California Institute of Technology, 1200 E. California Blvd., Pasadena, CA 91125, USA*

<sup>3</sup>*Herschel Science Centre, European Space Astronomy Centre, Villanueva de la Cañada, 28691 Madrid, Spain*

<sup>4</sup>*Institute for Astronomy, University of Edinburgh, Royal Observatory, Blackford Hill, Edinburgh EH9 3HJ, UK*

<sup>5</sup>*Laboratoire AIM-Paris-Saclay, CEA/DSM/Irfu - CNRS - Université Paris Diderot, CE-Saclay, pt courrier 131, F-91191 Gif-sur-Yvette, France*

<sup>6</sup>*Jet Propulsion Laboratory, 4800 Oak Grove Drive, Pasadena, CA 91109, USA*

<sup>7</sup>*Laboratoire d'Astrophysique de Marseille, OAMP, Université Aix-marseille, CNRS, 38 rue Frédéric Joliot-Curie, 13388 Marseille cedex 13, France*

<sup>8</sup>*Instituto de Astrofísica de Canarias (IAC), E-38200 La Laguna, Tenerife, Spain*

<sup>9</sup>*Departamento de Astrofísica, Universidad de La Laguna (ULL), E-38205 La Laguna, Tenerife, Spain*

<sup>10</sup>*Astrophysics Group, Imperial College London, Blackett Laboratory, Prince Consort Road, London SW7 2AZ, UK*

<sup>11</sup>*Department of Physics & Astronomy, University of British Columbia, 6224 Agricultural Road, Vancouver, BC V6T 1Z1, Canada*

<sup>12</sup>*Dept. of Astrophysical and Planetary Sciences, CASA 389-UCB, University of Colorado, Boulder, CO 80309, USA*

<sup>13</sup>*Observational Cosmology Lab, Code 665, NASA Goddard Space Flight Center, Greenbelt, MD 20771, USA*

<sup>14</sup>*Cardiff School of Physics and Astronomy, Cardiff University, Queens Buildings, The Parade, Cardiff CF24 3AA, UK*

<sup>15</sup>*Astronomy Centre, Dept. of Physics & Astronomy, University of Sussex, Brighton BN1 9QH, UK*

<sup>16</sup>*Dipartimento di Astronomia, Università di Padova, vicolo Osservatorio, 3, 35122 Padova, Italy*

<sup>17</sup>ESO, Karl-Schwarzschild-Str. 2, 85748 Garching bei München, Germany

<sup>18</sup>UK Astronomy Technology Centre, Royal Observatory, Blackford Hill, Edinburgh EH9 3HJ, UK

<sup>19</sup>Institut d’Astrophysique Spatiale (IAS), bâtiment 121, Université Paris-Sud 11 and CNRS (UMR 8617), 91405 Orsay, France

<sup>20</sup>Infrared Processing and Analysis Center, MS 100-22, California Institute of Technology, JPL, Pasadena, CA 91125, USA

<sup>21</sup>School of Physics and Astronomy, The University of Manchester, Alan Turing Building, Oxford Road, Manchester M13 9PL, UK

<sup>22</sup>Institut d’Astrophysique de Paris, UMR 7095, CNRS, UPMC Univ. Paris 06, 98bis boulevard Arago, F-75014 Paris, France

<sup>23</sup>Space Science & Technology Department, Rutherford Appleton Laboratory, Chilton, Didcot, Oxfordshire OX11 0QX, UK

<sup>24</sup>Institute for Space Imaging Science, University of Lethbridge, Lethbridge, Alberta, T1K 3M4, Canada

<sup>25</sup>Centre for Astrophysics Research, University of Hertfordshire, College Lane, Hatfield, Hertfordshire AL10 9AB, UK

<sup>26</sup>Mullard Space Science Laboratory, University College London, Holmbury St. Mary, Dorking, Surrey RH5 6NT, UK

**The extragalactic background light at far-infrared wavelengths<sup>1-3</sup> originates from optically-faint, dusty, star-forming galaxies in the universe with star-formation rates at the level of a few hundred solar masses per year<sup>4</sup>. Due to the relatively poor spatial resolution of far-infrared telescopes<sup>5,6</sup>, the faint sub-millimetre galaxies are challenging to study individually. Instead, their average properties can be studied using statistics such as the angular power spectrum of the background intensity variations<sup>7-10</sup>. A previous attempt<sup>11</sup> at measuring this power spectrum resulted in the suggestion that the clustering amplitude is below the level computed with a simple ansatz based on a halo model<sup>12</sup>. Here we report a clear detection of the excess clustering over the linear prediction at arcminute angular scales in the power spectrum of brightness fluctuations at 250, 350, and 500  $\mu\text{m}$ . From this excess, we find that sub-millimetre galaxies are located in dark matter halos with a minimum mass of  $\log[M_{\text{min}}/M_{\odot}] = 11.5^{+0.7}_{-0.2}$  at 350  $\mu\text{m}$ . This minimum dark matter halo mass corresponds to the most efficient mass scale for star formation in the universe<sup>13</sup>, and is lower than that predicted by semi-analytical models for galaxy formation<sup>14</sup>.**

Despite recent successes in attributing most of the extragalactic background light at sub-millimetre wavelengths to known galaxy populations through stacking analyses<sup>15-17</sup>, we have not individually detected the faint galaxies that are responsible for more than 85% of the total extragalactic intensity at these wavelengths<sup>18</sup>. The faint star-forming galaxies are expected to trace the large-scale structure of the Universe, especially in models where galaxy formation and evolution is closely connected to dark matter halos. While not individually detected in low resolution observations, the clustering of galaxies is expected to leave a distinct signature in the total intensity variations at sub-millimetre wavelengths. The amplitude of the power spectrum of intensity vari-

ations as a function of the angular scale provides details on the redshift distribution and the dark matter halo mass scale of dusty, star-forming galaxies in the universe<sup>7</sup>.

For this analysis, we used data from the Herschel Multi-tiered Extra-galactic survey (HerMES<sup>18</sup>), taken with the Spectral and Photometric Imaging Receiver (SPIRE<sup>19</sup>) onboard the *Herschel* Space Observatory<sup>20</sup>, during the *Science Demonstration Phase* (SDP) of *Herschel*. The data are composed of a wide 218' by 218' area in the Lockman Hole complemented by a narrow, but very deep (30 repeated scans), map of the Great Observatories Origins Deep Survey (GOODS) North field covering 30' by 30'. These fields have been very well studied at other wavelengths and they are known to have a low Galactic dust density, making it easier to distinguish the extragalactic component we wish to study. The observing time to complete each of the two fields was about 13.5 hours, observing simultaneously at 250, 350, and 500  $\mu\text{m}$ .

To limit the influence of a few bright galaxies on the measurement of the power spectrum, we removed galaxies brighter than 50 mJy in all three passbands by masking pixels in our maps with values larger than 50 mJy/beam as well as the neighboring pixels. We use the cross-power spectrum of two sub-maps as our estimate of the sky power spectrum to remove the contribution from the instrumental noise and alleviate potential systematic effects. We correct the raw cross-power spectra for the effects of the angular response function of the instrument and the transfer function of the map-making process. The angular response is established from a different set of SPIRE observations targeting Neptune, a strong point-like source for SPIRE, and involving a fine sampling of the beam with a total of 700 scans<sup>21</sup>. The effects of filtering of the time-ordered data and of the map pixelization are captured with a large set of sky simulations. To estimate our uncertainties, we propagate the errors from the beam measurement, while the simulations provide us with the instrumental and sky variance. The quadratic sum of these errors constitutes our error estimate.

The measured angular power spectrum (c.f. Figure 1a) contains contributions from spatial variations in Galactic dust clouds, or cirrus, brightness at large angular scales, the clustering of galaxies at intermediate angular scales, and a white-noise component at small angular scales arising from the Poisson behavior of the faint galaxies<sup>7,9</sup>. The cirrus signal in our Lockman-SWIRE field is taken from existing measurements in the same field with *IRAS* 100  $\mu\text{m}$  and MIPS<sup>22</sup> and extend this spectrum from 100  $\mu\text{m}$  to SPIRE wavelengths using the spectral dependence of a Galactic dust model<sup>23</sup>. We remove this cirrus power spectrum from our measurements and account for the uncertainty of the cirrus power spectrum by adding its error in quadrature to errors of our power spectrum points.

The Poisson behaviour of sources lead to an additional term to the angular power spectrum that is scale independent. The clustering component we measure is the excess of clustered background fluctuations above this shot-noise level. As the confusion noise is at the level of 6 mJy at SPIRE wavelengths<sup>5</sup>, with fluctuations in the brightness of the background we are probing the

clustering of faint galaxies with fluxes at the level of a few mJy at 350  $\mu\text{m}$ . To extract astrophysical information on faint galaxies from the clustering power spectrum we make use of the halo model<sup>12</sup>. This phenomenological approach connects the spatial distribution of galaxies in the universe to that of the dark matter. To model sub-millimetre galaxies in dark matter halos, we take a halo occupation distribution describing the number of galaxies as a function of the halo mass  $M$  of  $N_{\text{gal}}(M) = 1 + (M/M_1)^\alpha$  when  $M > M_{\text{min}}$  above the minimum mass scale  $M_{\text{min}}$ ,  $M_1$  is the mass scale at which more than one galaxy is present in a single dark matter halo, taken to be between 10 to 25 times  $M_{\text{min}}$ , and  $\alpha$  is the power-law scaling of satellite galaxies with halo mass. The halo model involves two parts with clustering of galaxies within halos, the one-halo term, and clustering of galaxies between halos, the two-halo term. While with the two-halo term alone parameters related to the occupation number are degenerate with each other and the bias factor or the number density of galaxies, with clustering in the one-halo part of the power spectrum also included the parameter degeneracies are broken and  $M_{\text{min}}$  can be determined more accurately<sup>12</sup>.

At scales of a few arcminutes and above we measure a clustering excess arising from the one-halo term and above the two-halo term tracing the linear density field power spectrum scaled by galaxy bias (c.f. Figure 1b). The one-halo term arises when more than one far-infrared galaxy occupies the same halo. While a hint of this one-halo term was previously seen in the clustering of the bright ( $> 30$  mJy) sub-millimetre galaxies<sup>27</sup>, evidence for such clustering was not present for bright galaxies in a different *Herschel* dataset<sup>24</sup>. To describe the power spectrum of the intensity fluctuations we also need a prescription for the redshift evolution of the source intensity. While models exist in the literature<sup>25,26</sup>, our data are of sufficient quality that we can directly constrain the redshift evolution of the source intensity from our measurements and we constrain its value in four redshift bins in the range 0 to 4.0. The halo model parameters, the source intensity parameters, and the shot-noise amplitude are jointly estimated with Markov-Chain Monte-Carlo fits to the power spectrum measurements. We impose an additional prior on our parameter estimates that the redshift integrated source intensity from our model fits, including the fractional contribution from bright sources that we have masked, be within the 68% range of the known background light intensity at each of the three wavebands<sup>2</sup>. We combine the estimates of the source intensity evolution at three wavebands of 250, 350 and 500  $\mu\text{m}$  and in four redshift bins to measure the bolometric luminosity density between 8 and 1100  $\mu\text{m}$  as a function of the redshift (c.f. Figure 2). We find that the far-infrared luminosity density continues to be significant out to a redshift of 4 and is at least a factor of 10 larger than the luminosity density of individually detected sub-mm sources with flux densities above 30 mJy alone<sup>18</sup>.

Using the halo model fits, we estimate the minimum dark matter mass scale for dusty star-forming galaxies at the peak of the star formation history of the universe to be  $\log_{10} M_{\text{min}}/M_\odot = 11.5_{-0.2}^{+0.7}$  at 350  $\mu\text{m}$  with a bias factor for the galaxies of  $2.4_{-0.2}^{+1.0}$ . The minimum halo masses  $\log_{10} M_{\text{min}}/M_\odot$  at 250 and 500  $\mu\text{m}$  are  $11.1_{-0.6}^{+1.0}$  and  $11.8_{-0.3}^{+0.4}$ , respectively. The corresponding bias factors for the galaxies are  $2.0_{-0.1}^{+0.9}$  and  $2.8_{-0.5}^{+0.4}$  at 250 and 500  $\mu\text{m}$ , respectively. The differences in the minimum halo masses and the bias factors between the three wavelengths are likely due a combination of effects including overall calibration uncertainties, the fact that at longer wave-

lengths we may be probing colder dust than at shorter wavelengths, and due to differences in the prior assumption on the total background intensity. In future, numerical models on the distribution of sub-millimetre galaxies will become useful to properly understand some of these subtle differences. Averaging over the three wavelengths the minimum halo mass for sub-millimetre galaxies is at the level of  $3 \times 10^{11} M_{\odot}$ , with an overall statistical uncertainty of roughly  $\pm 0.4$  in the logarithm of the minimum halo mass.

Based on a variety of observed scaling relations such as the one between stellar mass and circular velocity, the dark matter halo mass scale for efficient star-formation has been indirectly inferred to be about  $10^{11} M_{\odot}$ <sup>13</sup>. As the sub-millimetre galaxies are the most active star-forming galaxies in the universe, it is likely that the minimum halo mass scale for such galaxies that we determine from brightness fluctuations corresponds to the preferred mass scale of active star-formation in the universe. In dark matter halos below this mass, star-formation is expected to be inefficient due to photo-ionization feedback<sup>13</sup>. The underlying astrophysics needed to explain the numerical value we find are still missing in galaxy formation theories, since existing semi-analytical models predict a mass scale for faint sub-millimetre galaxies that are roughly ten times larger<sup>14</sup>. We provide the strongest evidence for a minimum mass scale for active star-forming galaxies in the universe by studying the background intensity variations generated by those galaxies in our sky maps. Our direct estimate of the minimum dark matter halo mass provides a critical value needed to improve theoretical models of sub-millimeter galaxies and the overall galaxy formation and evolution.

1. Puget, J.-L. et al. Tentative detection of a cosmic far-infrared background with COBE. *Astron. Astrophys.* 308, L5-L8 (1996).
2. Fixsen, D. J., Dwek, E., Mather, J. C., Bennett, C. L. & Shafer, R. A. The spectrum of the extragalactic far-infrared background from the COBE FIRAS observations. *Astrophys. J.* 508, 123-128 (1998).
3. Dwek, E. et al. The COBE Diffuse Infrared Background Experiment Search for the Cosmic Infrared Background. IV. Cosmological Implications, *Astrophys. J.* 508, 106-122 (1998).
4. Hughes, D. et al. High-redshift star formation in the Hubble Deep Field revealed by a submillimetre-wavelength survey, *Nature*, 394, 241-247 (1998).
5. Nguyen, H.T., et al. HerMES: The SPIRE confusion limit, *Astron. Astrophys.* 518, L5.1-L5.4 (2010).
6. Hauser, M. G., Dwek, E. The Cosmic Infrared Background: Measurements and Implications. *Ann. Rev. Astron. Astrophys.* 39, 249-307 (2001).
7. Amblard, A., Cooray, A. Anisotropy Studies of the Unresolved Far-Infrared Background. *Astrophys. J.* 670, 903-911 (2007).
8. Haiman, Z., Knox, L. Correlations in the Far-Infrared Background. *Astrophys. J.* 530, 124-132 (2000).

9. Knox, L., Cooray, A., Eisenstein, D., Haiman, Z. Probing Early Structure Formation with Far-Infrared Background Correlations. *Astrophys. J.* 550, 7-20 (2001).
10. Negrello, M. et al. Astrophysical and cosmological information from large-scale submillimetre surveys of extragalactic sources. *Mon. Not. R. Astron. Soc.* 377, 1557-1568 (2007).
11. Viero, M. P. et al. BLAST: Correlations in the Cosmic Far-Infrared Background at 250, 350, and 500  $\mu\text{m}$  Reveal Clustering of Star-forming Galaxies. *Astrophys. J.* 707, 1766-1778 (2009).
12. Cooray, A., Sheth, R. Halo models of large scale structure. *Phys. Rep.* 372, 1-129 (2002).
13. Bouché, N. et al. The Impact of cold gas accretion above a mass floor on galaxy scaling relations, *Astrophys. J.* 718, 1001-1018 (2010).
14. Gonzalez, J. E., Lacey, C. G., Baugh, C. M. & Frenk, C. S. The role of submillimetre galaxies in hierarchical galaxy formation, submitted to *Mon. Not. R. Astron. Soc.*, arXiv:1006.0230 (2010).
15. Devlin, J. M. et al. Over half of the far-infrared background light comes from galaxies at  $z \geq 1.2$ . *Nature* 458, 737-739 (2009).
16. Dole, H. et al. The cosmic infrared background resolved by Spitzer. Contributions of mid-infrared galaxies to the far-infrared background. *Astron. Astrophys.* 451, 417-429 (2006).
17. Marsden, G. et al. BLAST: resolving the cosmic submillimeter background. *Astrophys. J.* 707, 1729-1739 (2009).
18. Oliver, S. et al. HerMES: SPIRE galaxy number counts at 250, 350 and 500 microns, *Astron. Astrophys.* 518, L21.1-L21.4 (2010).
19. Griffin, M. J. et al. The Herschel-SPIRE instrument and its in-flight performance, *Astron. Astrophys.* 518, L3.1-L3.7 (2010).
20. Pilbratt, G. et al. Herschel Space Observatory - An ESA facility for far-infrared and submillimetre astronomy, *Astron. Astrophys.* 518, L1.1-L1.6 (2010).
21. Swinyard, B. et al. In-flight calibration of the Herschel-SPIRE instrument, *Astron. Astrophys.* 518, L4.1-L4.6 (2010).
22. Lagache, G. Bavouzet, N., Fernandez-Conde, N. et al. Correlated Anisotropies in the Cosmic Far-Infrared Background Detected by the Multiband Imaging Photometer for Spitzer: Constraint on the Bias. *Astrophys. J.* 665, L89-L92 (2007).
23. Schlegel, D. J., Finkbeiner, D. P., Davis, M. Maps of Dust Infrared Emission for Use in Estimation of Reddening and Cosmic Microwave Background Radiation Foregrounds. *Astrophys. J.* 500, 525-534 (1998).

24. Maddox, S.J. et al. Herschel ATLAS: The angular correlation function of submillimetre galaxies at high and low redshift, *Astron. Astrophys.* 518, L11.1-L11.4 (2010).
25. Lagache, G., Dole, H. & Puget, J.-L. Modelling the infrared galaxy evolution using a phenomenological approach, *Mon. Not. R. Astron. Soc.* 338, 555-571 (2003).
26. Valiante, E. et al. A Backward Evolution Model for Infrared Surveys: The Role of AGN- and Color- $L_{\text{TIR}}$  Distributions. *Astrophys. J.* 701, 1814-1838 (2009).
27. Cooray, A. 2010, HerMES: Halo Occupation Number and Bias Properties of Dusty Galaxies from Angular Clustering Measurements. *Astron. Astrophys.* 518, L22.1-L22.4 (2010).
28. Amblard, A. et al. Herschel-ATLAS: Dust temperature and redshift distribution of SPIRE and PACS detected sources using submillimetre colours *Astron. Astrophys.* 518, L9.1-L9.4 (2010).
29. Glenn, J. et al. HerMES: Deep Galaxy Number Counts from a P(D) Fluctuation Analysis of SPIRE Science Demonstration Phase Observations, *Mon. Not. R. Astron. Soc.* 409, 109-121 (2010).
30. Kennicutt, R. C. Jr. Star Formation in Galaxies Along the Hubble Sequence, *Ann. Rev. of Astron. Astrophys.* 36, 189-232 (1998).

**Acknowledgements** SPIRE has been developed by a consortium of institutes led by Cardiff University (UK) and including Univ. Lethbridge (Canada); NAOC (China); CEA, LAM (France); IFSI, Univ. Padua (Italy); IAC (Spain); Stockholm Observatory (Sweden); Imperial College London, RAL, UCL-MSSL, UKATC, Univ. Sussex (UK); and Caltech/JPL, IPAC, Univ. Colorado (USA). This development has been supported by national funding agencies: CSA (Canada); NAOC (China); CEA, CNES, CNRS (France); ASI (Italy); MCINN (Spain); SNSB (Sweden); STFC (UK); and NASA (USA). We thank M. Viero for useful comments. Amblard, Cooray, Serra, Khostovan, Mitchell-Wynne, and other US co-authors are supported by NASA funds for US participants in *Herschel* through an award from JPL. The data presented in this paper are publicly available from the ESA/Herschel Science Archive (<http://herschel.esac.esa.int>) under the observational identifications 1342186108, 1342186109, and 1342185536. Derived products by the HerMES collaboration, such as source catalogs, will be released through the HeDaM Database (<http://hedam.oamp.fr/HerMES>).

**Author Contributions** This paper represents the combined work of the HerMES Collaboration, the SPIRE Instrument Team's Extragalactic Survey, and has been extensively internally reviewed. A.C. planned the study, supervised the research work of A.A. and P.S. and wrote the draft version of this paper. A.A. performed the power spectrum measurements and P.S. interpreted those measurements with the halo model. All other coauthors of this paper contributed extensively and equally by their varied contributions to the SPIRE instrument, Herschel Mission, analysis of SPIRE and HerMES data, planning of HerMES observations, scientific support of HerMES, and by commenting on this manuscript as part of an internal review process.

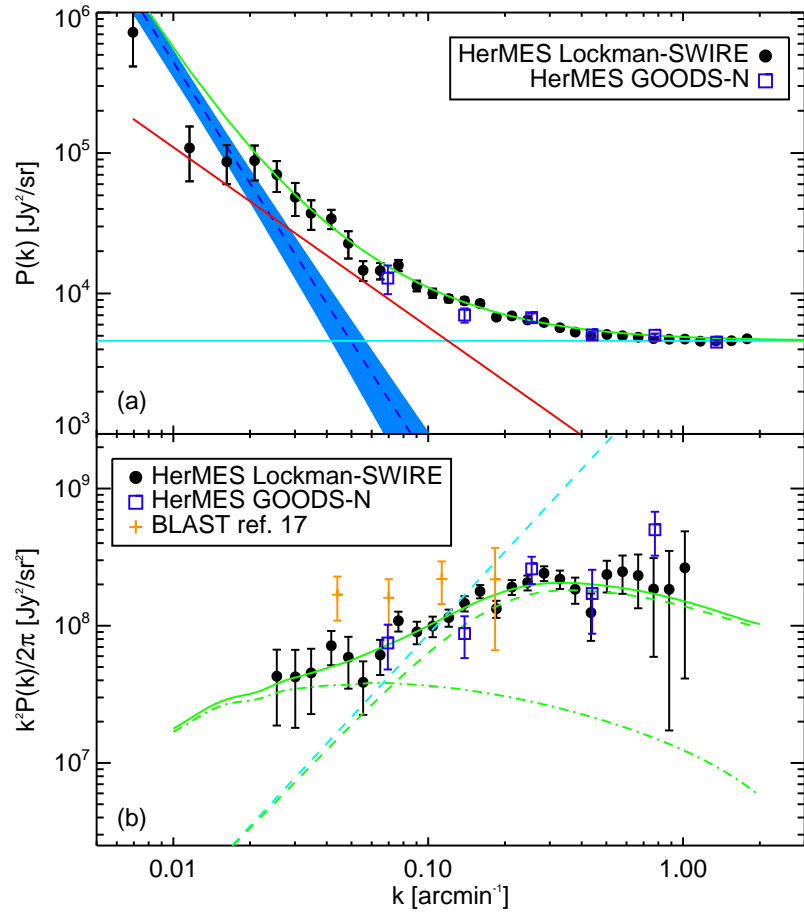
**Correspondence** Correspondence and requests for materials should be addressed to A.C. ([acooray@uci.edu](mailto:acooray@uci.edu))

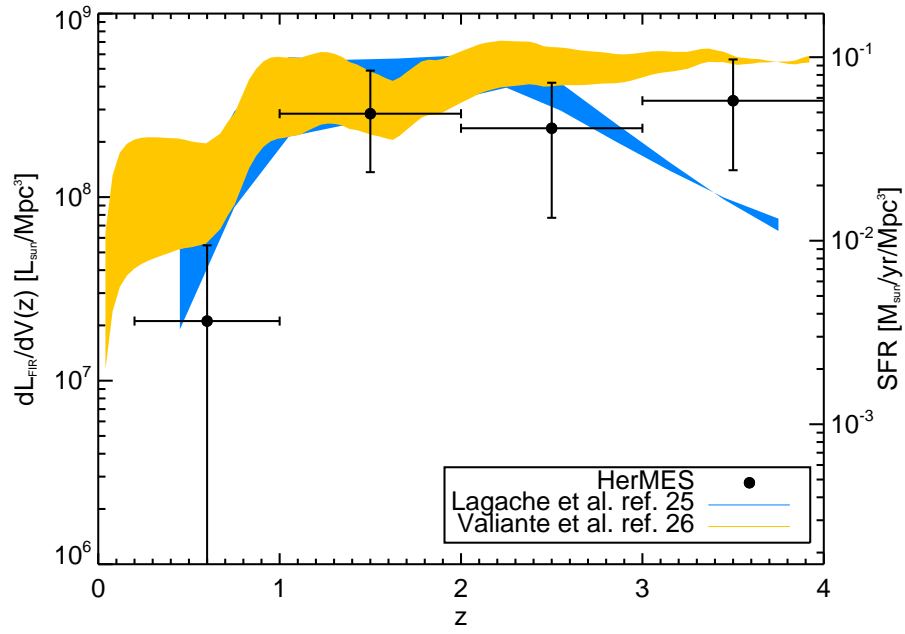
**Competing interests statement** The authors declare no competing interests.

**Supplementary information** accompanies this paper.

Figure 1: **The two-dimensional power spectrum of the Herschel map.** (a): The total power spectrum  $P(k)$  at  $350 \mu\text{m}$  as a function of the wavenumber  $k$  in  $\text{arcmin}^{-1}$ . The error bars are 68% confidence level uncertainties. The shaded region is the cirrus signal in our Lockman-SWIRE field. To describe the total power spectrum, we take a power-law with  $P(k) = A(k/k_1)^n + P_{\text{SN}}$  where  $k_1$  is fixed at  $0.1 \text{ arcmin}^{-1}$  and  $P_{\text{SN}}$  is the shot-noise amplitude. At  $350 \mu\text{m}$ , we find  $A = (5.79 \pm 0.26) \times 10^3 \text{ Jy}^2/\text{sr}$  and  $n = -1.28 \pm 0.07$ , shown by the red-line. The light blue line is the best-fit shot-noise amplitude with a value of  $4600 \pm 70 \text{ Jy}^2/\text{sr}$ , in agreement with the value of  $4500 \pm 220 \text{ Jy}^2/\text{sr}$  predicted by best determined source counts<sup>29</sup>. The shot-noise errors include the 15% uncertainty in the SPIRE absolute flux calibration<sup>21</sup>. In green we show the total power spectrum combined with the mean estimate of the cirrus signal. (b): The angular clustering power spectrum at  $350 \mu\text{m}$  as a function of the wavenumber with errors showing the 68% confidence level uncertainties. The best-fit shot-noise value (dashed blue line) has been removed from the data and its uncertainty added to the overall error in quadrature. The green lines show the best-fit halo model with a reduced chi-square value of 1.02. The dot-dashed line show the two-halo term and the dashed line show the one-halo term that is responsible for the clustering at small angular scales. Data in the lowest wavenumber bins contaminated by the Galactic cirrus have been omitted. For comparison we also show a previous measurement of the power spectrum of brightness fluctuations at  $350 \mu\text{m}$  with BLAST<sup>11</sup>. The results related to 250 and 500  $\mu\text{m}$  are summarized in the Supplementary Information.

Figure 2: **Far-infrared bolometric luminosity density (between 8 and 1110  $\mu\text{m}$ ) and star formation rate as a function of redshift.** The far-infrared bolometric luminosity density was estimated using the values of the source intensity in four redshift bins between 0 and 4 derived from best-fit model fits to each of the power spectra from the three wavebands and with a prior selection of models with  $\alpha > 1$  for the power-law slope of the occupation number. We have assumed a modified black-body spectrum for the spectral energy distribution of the spatially unresolved sources, with an emissivity index of 1.5 and a dust temperature of  $28 \pm 8 \text{ K}$ <sup>28</sup>. We propagate the uncertainty on the dust temperature as an additional error when computing errors on the luminosity density in each of the redshift bins. The vertical bars show the 68% confidence level errors propagated from errors in the source intensity evolution estimates and from the temperature prior, while the horizontal bars indicated the redshift range of each of the bins we use for model fits. The orange and blue shaded areas represent the model from Lagache et al.<sup>25</sup> and Valiante et al.<sup>26</sup> with the same flux cut ( $S > 50 \text{ mJy}$ ) and the same temperature prior as our data. Our measurements are consistent with both these models. The redshift evolution of the far-infrared luminosity is a measure of the star formation history of the universe<sup>30</sup> and converting our estimate, we find a star formation rate of  $< 0.01$ ,  $0.05 \pm 0.03$ ,  $0.04 \pm 0.03$ , and  $0.06 \pm 0.04 \text{ M}_\odot/\text{yr}/\text{Mpc}^3$  in each of the redshift bins of  $z < 1$ ,  $1 < z < 2$ ,  $2 < z < 3$ , and  $3 < z < 4$ , respectively.





In these Supplemental Notes to our main paper, we outline key details related to how we estimated the angular power spectrum of *Herschel*-SPIRE data and its interpretation.

The data presented in the main paper are publicly available from the ESA/Herschel Science Archive (<http://herschel.esac.esa.int>) under the observational identifications 1342186108, 1342186109, and 1342185536. Derived products by the HerMES collaboration, such as source catalogs, will be released through the HeDaM Database (<http://hedam.oamp.fr/HerMES>).

**Data Analysis and Map making:** The data were taken in the standard Scan-Map AOT for which the scanning speed is 30"/s. Calibrated time-ordered data were created using HIPE<sup>31</sup> development version 2.0.905, with a fix applied to the astrometry (included in more recent versions of the pipeline), with newer calibration files (SPIRE Beam Steering Mirror calibration version 2, flux conversion version 2.3 and temperature drift correction version 2.3.2) and with a median slope subtracted from each timeline. We removed a few percent of the data samples which were contaminated by cosmic-rays or instrumental effects and flagged by the initial pipeline.

We convert time-ordered data to a map on the sky through an iterative baseline removal and an iterative calculation of detector weights. We give a summary of the map-making method here. Full details of this approach is available elsewhere<sup>32,34</sup>.

Given sky brightness  $I(\theta)$ , the signal for a detector  $d$  in a scan  $s$  with a time sample  $j$  can be written as

$$S_{dsj} = I(\theta_{dsj}) + P_{ds}^n + N_{dsj}, \quad (1)$$

where  $P_{ds}^n$  is an  $n$ -th order polynomial baseline offset for detector  $d$  and scan  $s$ , and  $N_{dsj}$  is the instrumental noise. The parameters of  $P_{ds}^n$  are solved with an iterative solution to the best-intensity of the sky at each step.

At each iteration  $i$ , we minimize the variance of the residual  $V_{dsj}^i$  based on the previous map  $I^{i-1}(\theta_{dsj})$  such that

$$V_{dsj}^i = S_{dsj} - [I^{i-1}(\theta_{dsj}) + P_{ds}^{n,i}]. \quad (2)$$

The  $i$ -th estimate of the sky is performed via the weighted mean of all the samples that fall into a given pixel:

$$I^i(\theta) = \frac{\sum_{dsj} w_{ds}^i (S_{dsj} - P_{ds}^{n,i})}{\sum_{dsj} w_{ds}^i}. \quad (3)$$

The weight associated with each iterative estimate is simply the inverse variance of the residual

$$w_{ds}^i = \frac{N_{\text{tot}}}{\sum_{k=1}^{N_{\text{tot}}} (V_{dsj}^k)^2}. \quad (4)$$

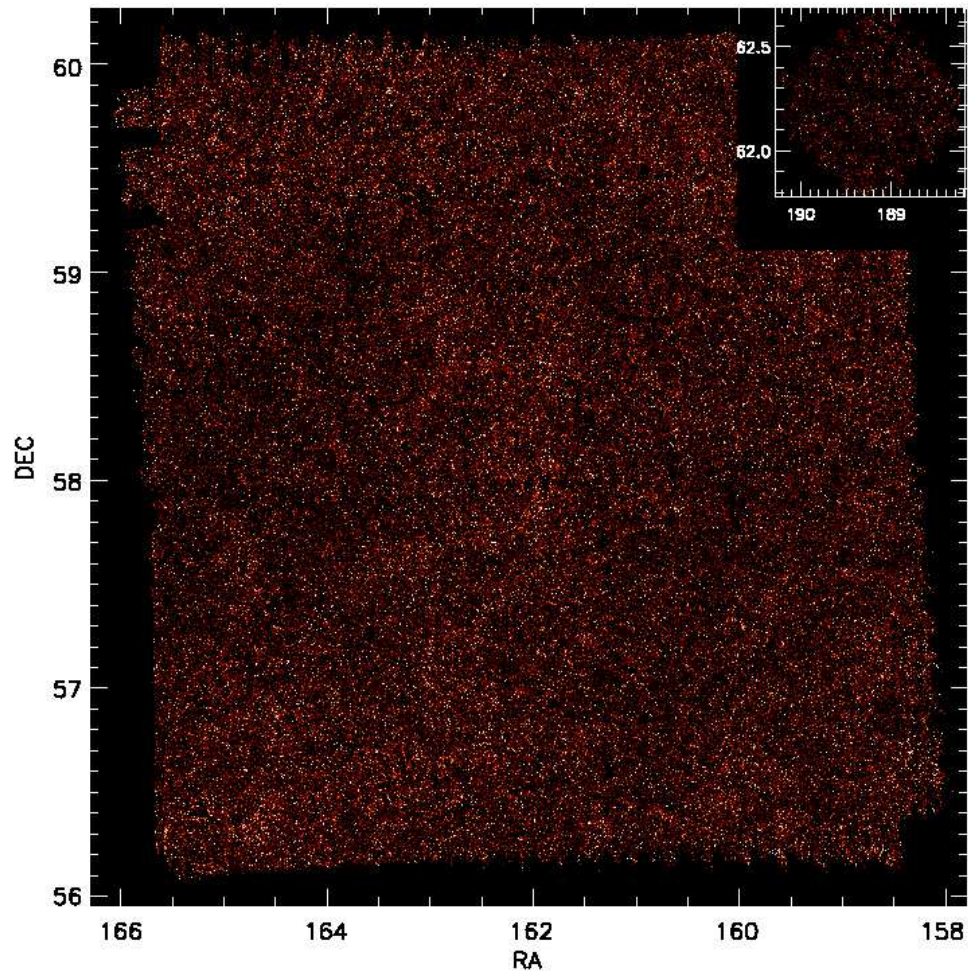


Figure S 1: **The 250  $\mu\text{m}$  SPIRE maps of Lockman-SWIRE and GOODS-N (top-right inset) fields.** We have masked all galaxies above 50 mJy.

The algorithm also allows us to create a noise map by propagating detector noise as estimated by the variance of the residuals. The maps used here make use of a first-order polynomial with  $n = 1$  and 20 iterations. The gain offsets were computed from the 1st iteration while the weights are fixed to 1.0 for the 10 iterations and are calculated from the data starting at iteration 11, to improve stability of the algorithm. The same procedure is repeated for both Lockman-SWIRE and GOODS-N maps and also iterative maps of Neptune that we use for beam measurements. The maps at  $250 \mu\text{m}$  are shown in Figure S1.

The absolute astrometry of the maps was corrected by stacking at the positions of *Spitzer* Multi-Band Imaging Photometer (MIPS)  $24 \mu\text{m}$  and radio sources, finding reasonably consistent results between the two within  $0.5''$ . We have made an overall correction to the absolute astrometry of the order of a few arcseconds, though such small angular scale corrections do not impact results we present here focusing between 0.5 arcminutes to 100 arcminutes.

The maps were made with pixels of size 6, 8.3, and 12 arcseconds at 250, 350,  $500 \mu\text{m}$ , respectively, corresponding to one third of the full-width at half-maximum (FWHM) of the SPIRE beam profiles<sup>33</sup> in the three passbands.

**Raw Power Spectra** To compute the power spectrum in our map, we use fast Fourier transforms; however, we need to take into account the missing and unwanted pixels. Due to our scanning strategy and some corrupted data, a small fraction of pixels are not defined on the map that we use to define our Fourier transform basis. Furthermore, we wish to remove the brightest galaxies in order to reduce the shot-noise term in the power spectrum, since the shot-noise term is weighted towards bright galaxies and larger shot-noise degrades the ability to extract the clustering component of the power spectrum. In our analysis we applied a flux cut of 50 mJy/beam, removing 0.9, 0.7, 1.2% of the pixels at 250, 350,  $500 \mu\text{m}$ , respectively, in the Lockman-SWIRE field and 0.5, 0.2, 0.2% in the GOODS-N field. We used the same flux cut at all frequencies for simplicity, this 50 mJy/beam allows to remove all the bright sources while retaining most of the pixels in each map. The remaining number of pixels used for the fluctuation study is  $5.4 \times 10^6$ ,  $2.9 \times 10^6$ , and  $1.4 \times 10^6$  at 250, 350,  $500 \mu\text{m}$ , respectively, in the Lockman-SWIRE field and  $1.9 \times 10^5$ ,  $1.0 \times 10^5$ ,  $4.7 \times 10^4$  in the GOODS-N field.

The raw power spectra are summarized in Figure S2. Here, we show the auto spectra in the total map as well as the cross spectrum with maps made with half of the time-ordered data in each map. The difference of the two provides us with an estimate of the instrumental noise. At small physical scales (large  $k$  values) the noise is almost white such that  $P(k)$  is a constant value. We fit a model of the form

$$N(k) = N_0 \left[ \left( \frac{k_0}{k} \right)^2 + 1 \right], \quad (5)$$

and determine the knee scale of the noise,  $k_0$ , to be at about  $0.15 \text{ arcmin}^{-1}$  at each of 250, 350, and  $500 \mu\text{m}$ .

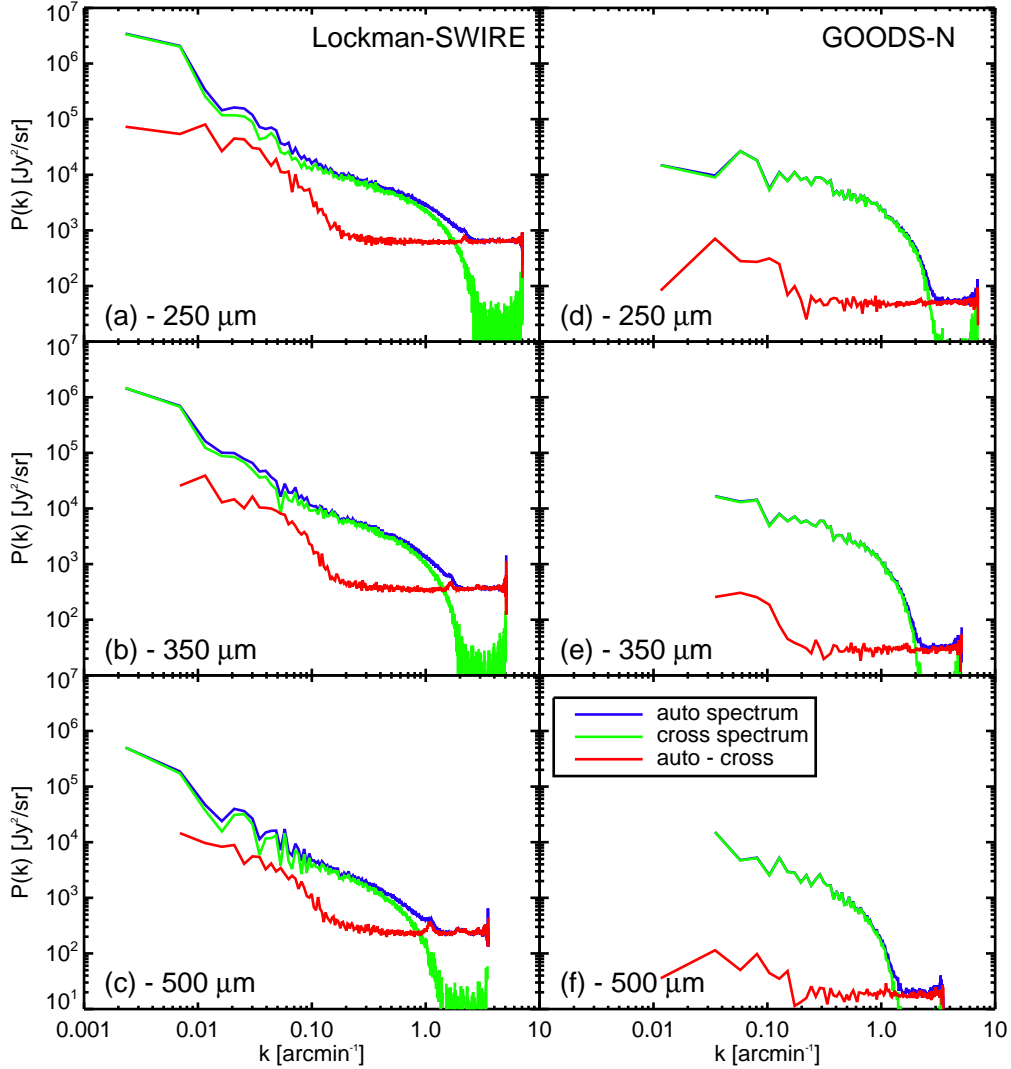


Figure S 2: **Raw  $P(k)$  of the Lockman-SWIRE (left) and GOODS-N (right) fields.** The panels show the three wavebands with  $250 \mu\text{m}$  (panels *a* and *d*),  $350 \mu\text{m}$  (*b* and *e*), and  $500 \mu\text{m}$  (*c* and *f*) from top to bottom on each side, respectively. The blue lines show the auto-power spectra computed from maps using all the data. This power spectrum is a combination of sky signal and instrumental noise. We estimate the sky signal through the cross-spectrum (green lines) of two maps after dividing the data into two halves separated in time. The difference of these two spectra represents an estimate of the instrumental noise power spectrum (red line).

**Corrected Power Spectra:** The final power spectrum we show in this paper is corrected for a combination of effects described by

$$P(k') = B(k)T(k)M_{k'k}P(k), \quad (6)$$

where  $P(k')$  is the observed power spectrum from data in the presence of mask,  $B(k)$  is the beam function, and the map making transfer function is  $T(k)$ .  $P(k)$  is the true sky power spectrum and is determined by inverting the above equation.

In the above,  $M_{kk'}$  is the mode coupling matrix associated with the mask. This can be expressed analytically in the flat sky approximation<sup>35</sup> as

$$M_{kk'} = \sum_{\theta_k} \sum_{\theta_{k'}} |w(k - k')|^2 / N(\theta_k), \quad (7)$$

where  $w(k)$  is the Fourier transform of the mask. Figure S3 shows the mask we used and the corresponding matrix  $M_{kk'}$  for each of Lockman-SWIRE and GOODS-N fields at 250  $\mu\text{m}$  with sources above 50 mJy and spurious data removed.

We measure the beam function  $B(k)$  through observations of Neptune, involving a total of 700 scans. Figure S4 shows the Neptune maps made at 250, 350, and 500  $\mu\text{m}$ . The Neptune data are analyzed in the same manner as the Lockman-SWIRE and GOODS-N data using the same iterative map maker. In addition we also employ a naive map maker available as part of HIPE<sup>31</sup>. When making these maps, we account for the relative motion of Neptune relative to the background sky and make maps that correct for Neptune's varying position during the observations. This results in a map where extragalactic sources are smeared. Neptune, however, is several orders of magnitude brighter and our beam measurements primarily focus on the central region. Figure S5 summarizes the results related to  $B(k)$  for each of the three SPIRE wavelengths. In the same figure (bottom panels), we also compare the beam measured from Neptune to the beam described by a Gaussian with a FWHM of 18, 25, and 36'' at 250, 350, and 500  $\mu\text{m}$ . The amplitude of  $B(k)$  is thereafter interpolated in the  $k$  modes at which we compute our fluctuation power spectra.

The uncertainty in the beam function  $B(k)$  is determined by computing the standard deviation of the different  $B(k)$  estimates, using the measurements on the iterative and naive map and several different interpolation schemes. The beam uncertainty computed this manner is slightly larger than the difference in the beams between two different observations of Neptune, one involving the fine scans we primarily use here and an older coarse set of Neptune scans, but with maps made using the same map-maker. Figure S6 shows the overall uncertainties in the beam (solid lines) as well as the uncertainties coming from the difference between the naive and iterative map reconstructions (dashed lines). Figure S7 compares the beam function and the power spectrum  $P(k)$  at 250  $\mu\text{m}$  from the Lockman-SWIRE field showing that features in the power spectrum are not related to features in the beam function  $B(k)$ .

To measure the transfer function  $T(k)$  associated with the map maker, we realize 100 simu-

lations of a first estimate of our beam-convolved power spectrum and pass it through the iterative map-making pipeline used to reduce our real data. We then compute the average of the ratio between the estimated spectrum and the input spectrum with simulated maps masked exactly as in the real sky maps. This function is the transfer function  $T(k)$  of the map-making pipeline associated with median filter and other filtering (Figure S8). We divide the estimated power spectrum by this transfer function to remove the map making pipeline processing effects.

**Total error budget:** The total error budget in our clustering plots is composed of three contributions involving the uncertainty of the beam, uncertainty in the shot-noise determination, and the instrumental noise error. The latter is computed from simulations while the beam error comes from the differences in our estimates of the beam. Shot-noise error results from direct fits to the measured data points. Figure S9 summarizes the error budget as a function of wave number and also compares the instrumental noise error to an analytical formula for its expectation<sup>36</sup>.

While in Figure 1 of the main paper we showed  $P(k)$  at  $350 \mu\text{m}$ , in Figure S10 we show the same at  $250$  and  $500 \mu\text{m}$ .

**Jack-knife tests:** The results shown in this study were obtained by dividing the data into two equal and consecutive halves and by taking the cross-power spectrum of the resultant maps. We can make the same cross-correlation power spectrum measurements and repeat the whole process with maps made by dividing data into several other combinations. To be specific, we divide the data into four pieces, each filling approximately our total field, and use these to measure the cross-power spectrum for two other combinations namely  $[(1 + 3) \times (2 + 4)]$  and  $[(1 + 4) \times (2 + 3)]$ , where 1 to 4 are four equal subdivisions of data in time.

Figure S11 summarizes our results, showing that within the uncertainties we recover similar power spectra. Given the observing strategy, the  $(1 + 3)$  and  $(2 + 4)$  maps are each made with parallel scans, but roughly perpendicular to each other. The fact that we do not see a statistically significant difference shows that the beam ellipticity is not an important systematic concern in this study.

**Null tests:** In addition to the jack-knife tests with a variety of sub-maps with data divided to four intervals and all leading to a measurement of the sky signal, we also perform several null tests using data combinations that remove the sky signal. In this case, instead of computing the cross-power spectra of the sum maps of data combinations, we make use of the sub-maps made by taking the differences of data combinations, again data divided to four sub-intervals as the case of signal measurement. As an example, in Figure S12 we show the cross-power spectrum computed at  $250$ ,  $350$ , and  $500 \mu\text{m}$  with the  $(1 - 2)$  map cross-correlated against the  $(3 - 4)$  map. For reference, we also show the default power spectrum computed with  $[(1 + 2) \times (3 + 4)]$ .

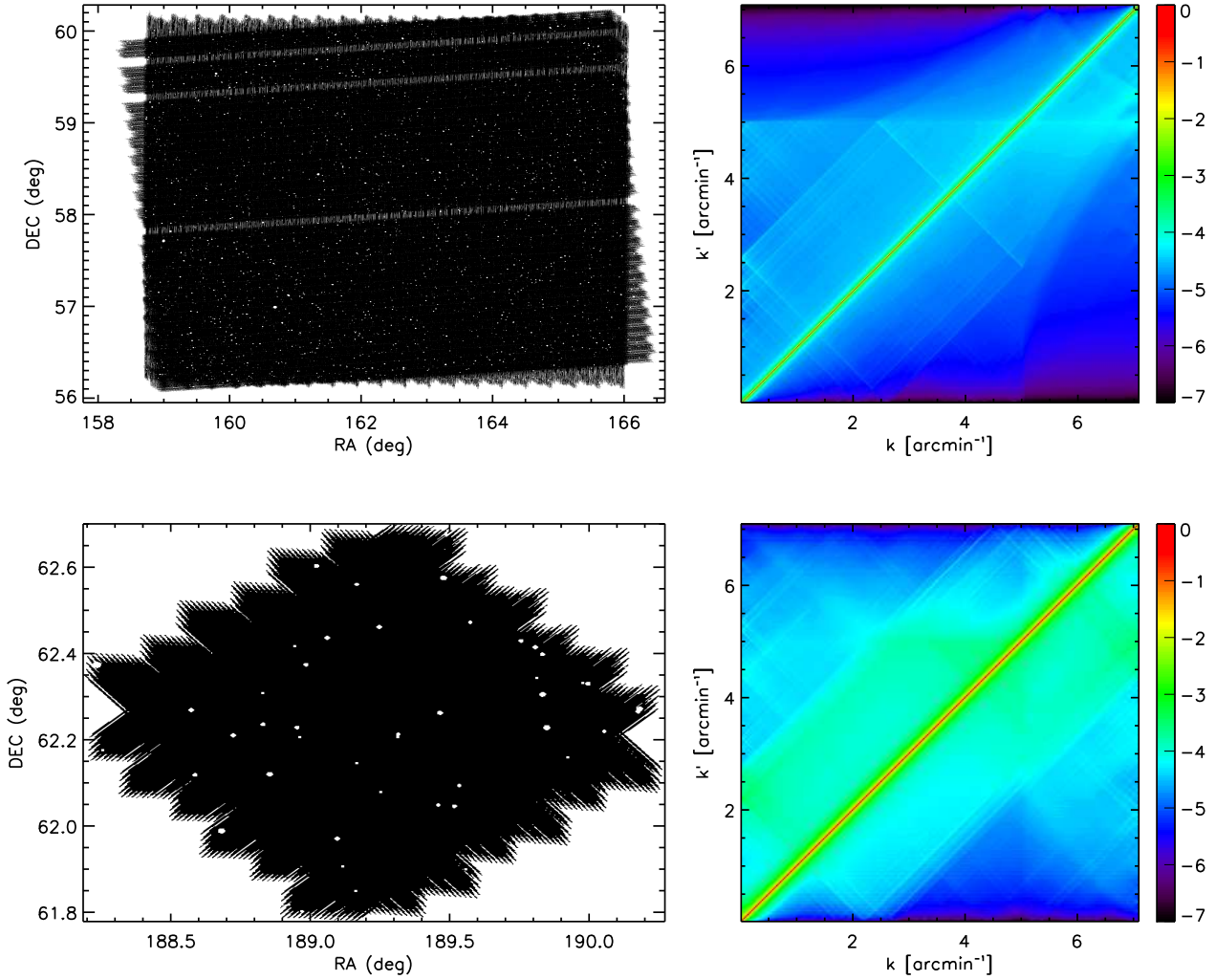


Figure S 3: **Mask and the model coupling matrix.** *Top-left* : Mask used for the Lockman-SWIRE field. The galaxies brighter than 50 mJy masked as well as some corrupted scans. *Top-right*: Coupling matrix  $M_{kk'}$  (log scale) computed for this Lockman-SWIRE mask. *Bottom-left* and *bottom-right* figures are the same things for the GOODS-N field.

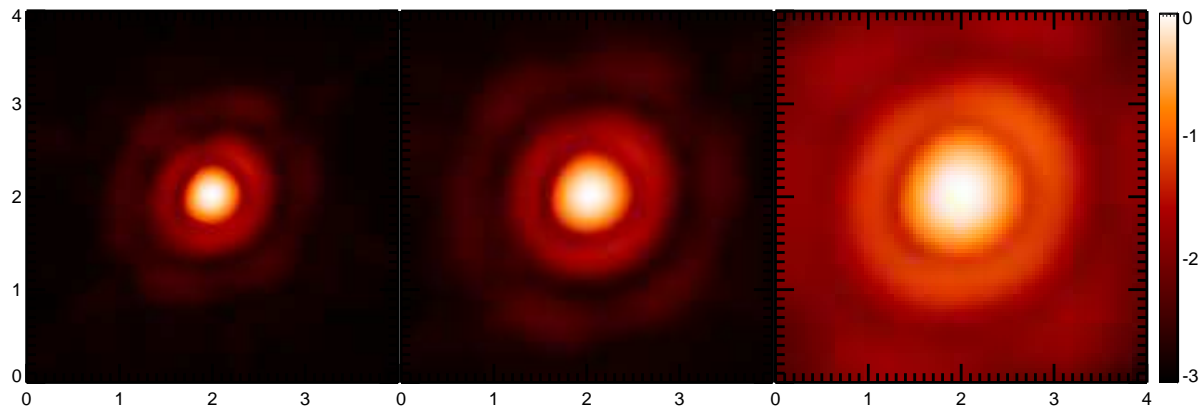


Figure S 4: **Maps used for the beam function measurements.** From left to right, Neptune beam maps (log scale normalized to the maximum) at 250, 350, and 500  $\mu\text{m}$ , respectively. The x- and y-axes are labeled in arcminutes. The maps were made with the iterative map-maker and observations involve a total of 700 scans of Neptune.

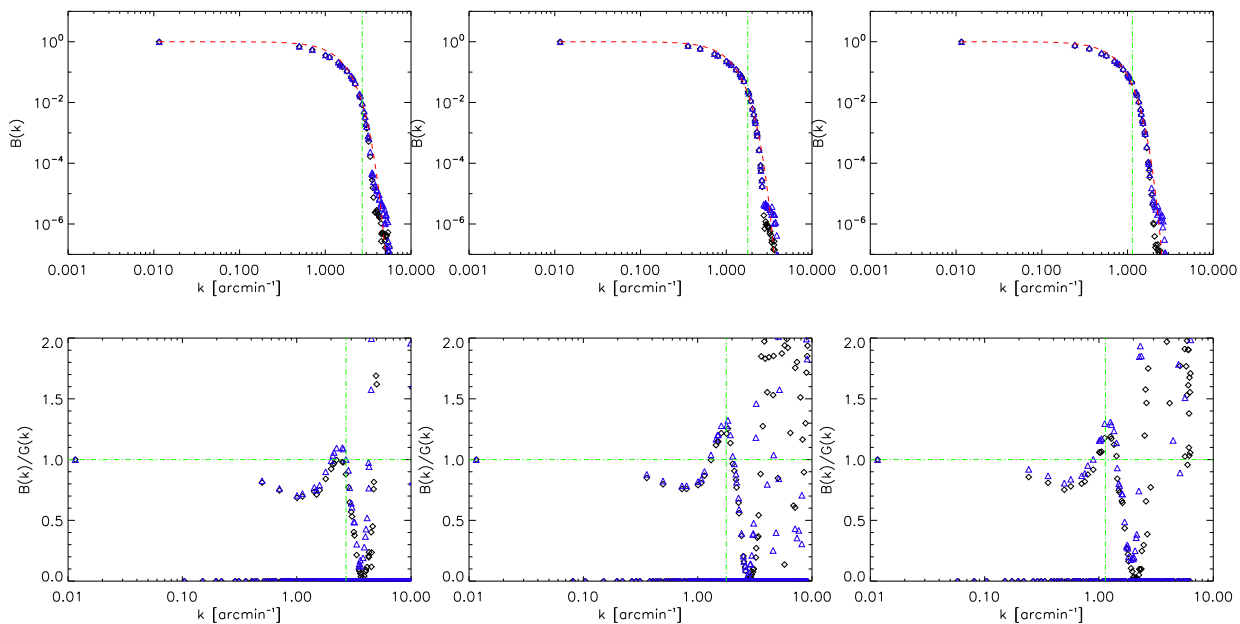


Figure S 5: **Point spread function of SPIRE Instrument.** **Top :** Point Spread Function Fourier space kernels for 250, 350 and 500  $\mu\text{m}$  (from left to right). The black diamonds were estimated using the Neptune “naive” map, the blue triangles with the Neptune “iterative” map and the red dashed line is the Gaussian (FWHM of 18, 25 and 36 arcseconds). The vertical green dashed dotted lines represent the maximum  $k$  out to which the data are used in this analysis. **Bottom:** Ratio of the beam kernel measured on Neptune to the Gaussian beam approximation.

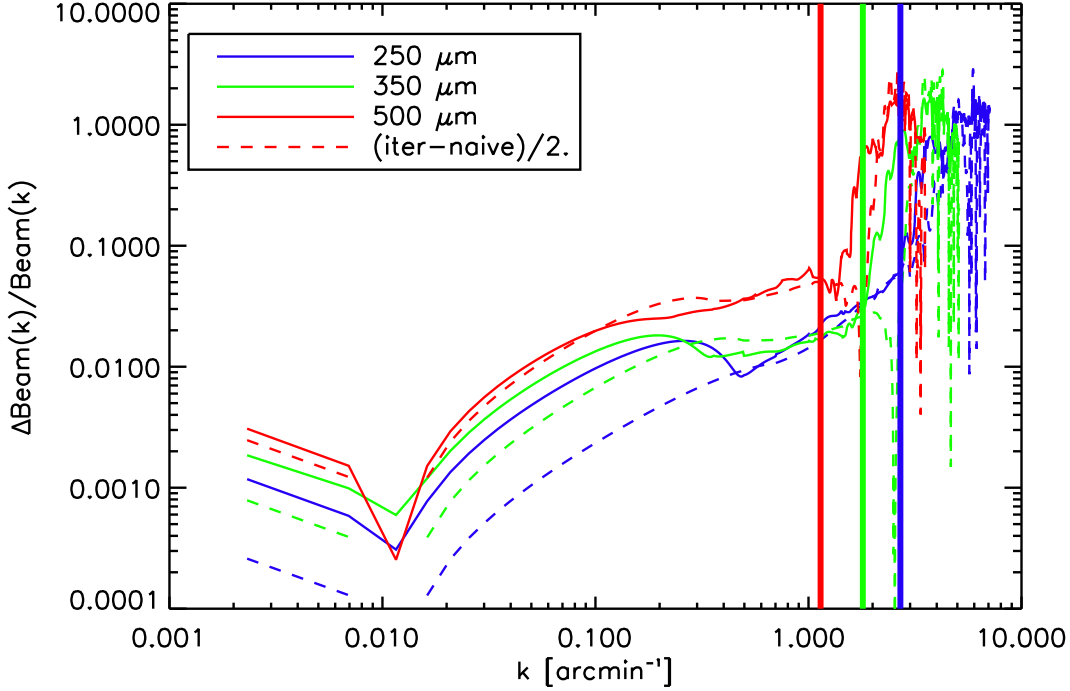


Figure S 6: **Accuracy of the beam measurement.** The beam uncertainty relative to the mean beam function used for this analysis. The total uncertainty (solid lines) is the standard deviation of the different  $B(k)$  estimates using the measurements on the iterative and naive map and several interpolation methods. The dashed lines are half of the difference between one of the naive map  $B(k)$  estimates and one of the iterative map  $B(k)$  estimates. The vertical lines mark the maximum  $k$  value out to which we make use of the power spectrum measurements at each of 250, 350, and 500  $\mu\text{m}$ .

Band	A ( $\text{Jy}^2/\text{sr}$ )	$n$	$P_{\text{SN}}$ ( $\text{Jy}^2/\text{sr}$ )	$\chi^2/\text{d.o.f.}$
250 $\mu\text{m}$	$(7.64 \pm 0.55) \times 10^3$	$-1.20 \pm 0.09$	$5798_{-132}^{+92}$	0.93
350 $\mu\text{m}$	$(5.79 \pm 0.26) \times 10^3$	$-1.28 \pm 0.07$	$4373_{-76}^{+62}$	1.03
500 $\mu\text{m}$	$(2.67 \pm 0.13) \times 10^3$	$-1.16 \pm 0.09$	$1700 \pm 80$	1.2

Table S 1: **Power-law best fit values at  $k_1 = 0.1 \text{ arcmin}^{-1}$ .**

Notes: To describe the power spectrum, we take a power-law with  $P(k) = A(k/k_1)^n + P_{\text{SN}}$  where  $k_1$  is fixed at  $0.1 \text{ arcmin}^{-1}$  and  $P_{\text{SN}}$  is the shot-noise amplitude, assuming a power-law fit to the data. The errors are 68% confidence level uncertainties determined from the MCMC fits.

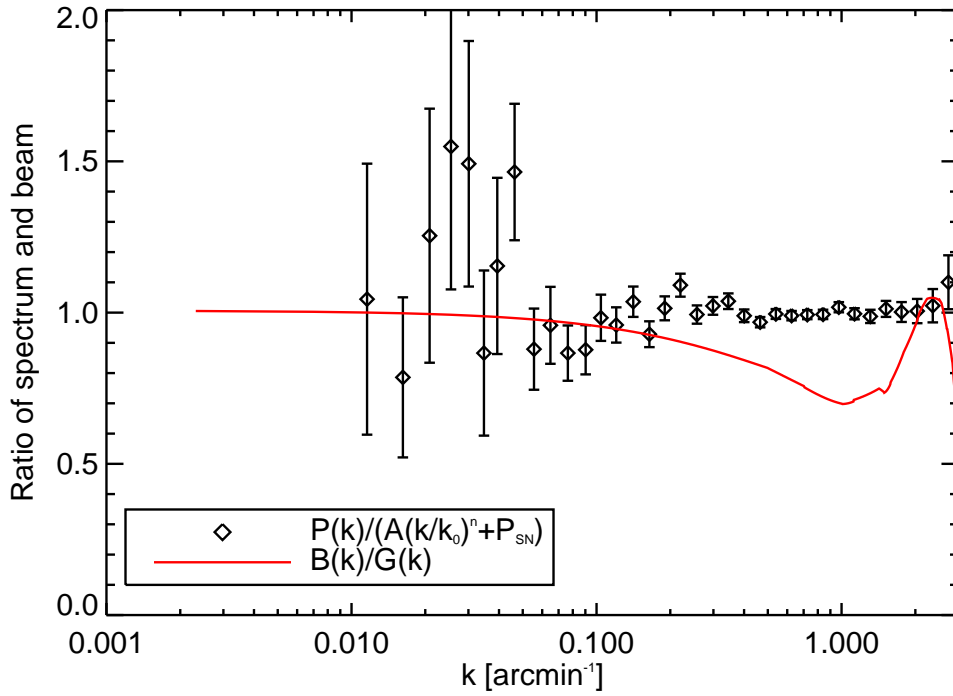


Figure S 7: **Power spectrum relative to the beam function.** Comparison of the  $P(k)$  estimate and the beam transfer function shape. The black diamonds represent our  $250 \mu\text{m}$   $P(k)$  estimate divided by the best fit power-law. The red line represents our beam transfer function divided by the approximate Gaussian beam. The two curves have different shapes and this difference indicates that the  $P(k)$  shape does not come from the beam transfer function.

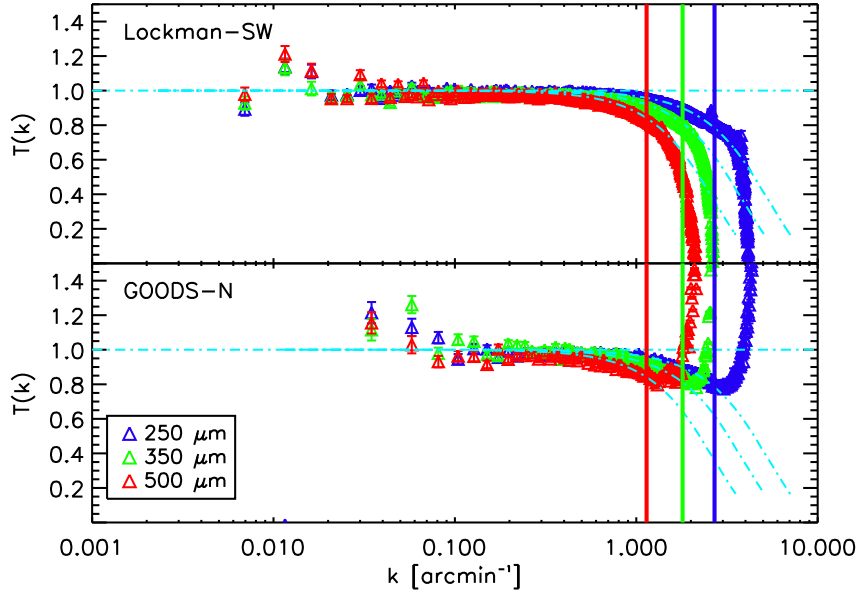


Figure S 8: **Map-making transfer function.** Transfer function  $T(k)$  due to the iterative map-maker and filtering on the cross-spectra of our two fields. The blue, green and red triangles represent, respectively, the transfer function at 250, 350 and 500  $\mu\text{m}$ .  $T(k)$  is essentially equal to 1 between 0.02 and 0.4  $\text{arcmin}^{-1}$ . The map-maker adds about 10% power around 0.01  $\text{arcmin}^{-1}$  in the case of Lockman-SWIRE (top panel) and around 0.05  $\text{arcmin}^{-1}$  in the case of GOODS-N (bottom panel) and reduces the power on small scales mostly by averaging the data into pixels (light blue dotted dashed lines). The vertical lines mark the maximum  $k$  out to which we make use of the power spectrum estimates for shot-noise and clustering measurements.

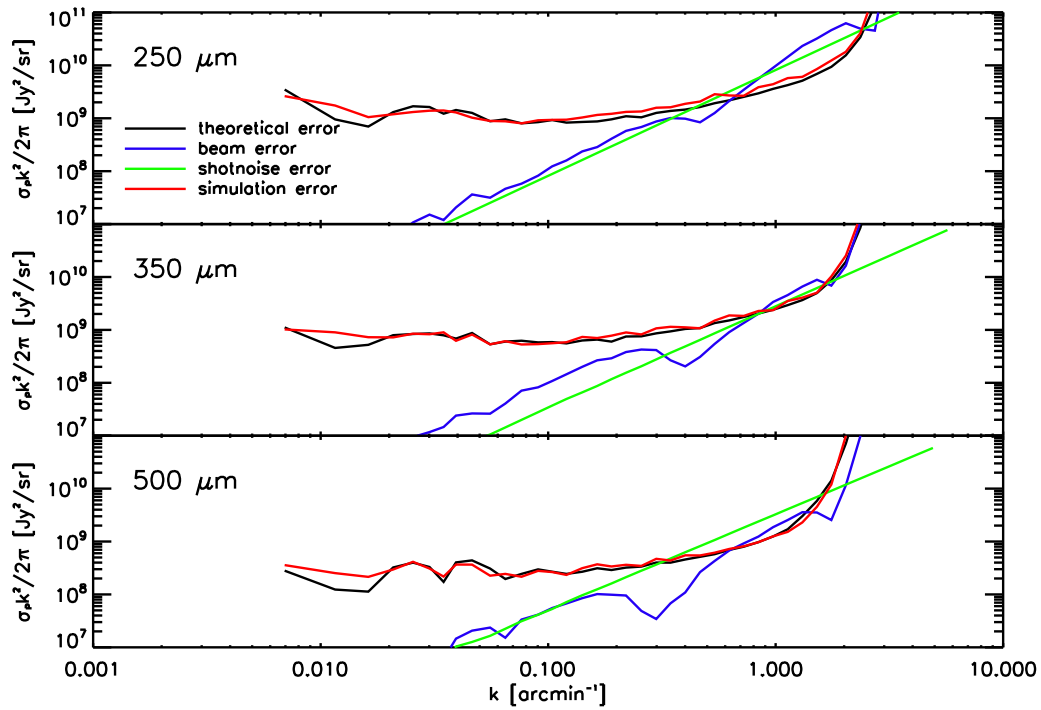


Figure S 9: **The power spectrum uncertainties.** Error budget at 250, 350, and 500  $\mu\text{m}$ . We show the error separated into the beam uncertainty (blue lines), the shot-noise determination (green lines), and the simulations (sky and instrumental variance, red lines). The simulation uncertainty is compared to an analytical noise estimate (black lines).

**Cirrus power spectrum** The cirrus signal in our Lockman-SWIRE field is taken from existing measurements in the same field with *IRAS* 100  $\mu\text{m}$  and MIPS<sup>39</sup> with a power spectrum,  $P(k)$ , of the form  $P_{\text{cirrus}}(k) = P_0(k/k_0)^\beta$  at 160  $\mu\text{m}$  with  $P_0 = (2.98 \pm 0.66) \times 10^6 \text{ Jy}^2/\text{sr}$  and  $\beta = -2.89 \pm 0.22$  when  $k_0 = 0.01 \text{ arcmin}^{-1}$ . We extend this spectrum from 100  $\mu\text{m}$  to SPIRE wavelengths using the spectral dependence of a Galactic dust model<sup>40</sup>.

	$\log[M_{\min}/M_{\odot}]$	$\alpha$	$\langle b \rangle_z$	$P_{\text{SN}} \text{ (Jy}^2/\text{sr)}$	$\chi^2/\text{d.o.f.}$
250 $\mu\text{m}$	$11.1^{+1.0}_{-0.6}$	$1.6^{+0.1}_{-0.2}$	$2.0^{+0.9}_{-0.1}$	$6100 \pm 120$	0.76
350 $\mu\text{m}$	$11.5^{+0.7}_{-0.2}$	$1.8^{+0.1}_{-0.7}$	$2.4^{+1.0}_{-0.2}$	$4600 \pm 70$	1.02
500 $\mu\text{m}$	$11.8^{+0.4}_{-0.3}$	$1.8^{+0.1}_{-0.7}$	$2.8^{+0.4}_{-0.5}$	$1800 \pm 80$	1.44

Table S 2: **Halo model best fit values from the measured power spectra at the three wavebands.**

We tabulate the best-fit values with 68% confidence level errors for halo occupation number used to interpret the power spectrum measurements. The average galaxy bias factor is  $\langle b \rangle_z$ .  $P_{\text{SN}}$  is the amplitude of shot-noise fluctuations, also jointly determined from the power spectra as part of our model fitting process. The errors of the shot-noise amplitudes  $P_{\text{SN}}$  include an extra error corresponding to the uncertainty of the absolute flux calibration scale at the three SPIRE wavebands of 15%<sup>33</sup>. The chi-square values of the best-fit model, per degree-of-freedom, are also tabulated. We do not tabulate the values of  $M_1$  as it remains unconstrained within the prior of  $M_1/M_{\min}$  taken to be between 10 and 25.

**Interpretation Model** In Table S1 we summarize results related to power-law model fits with  $P(k) = A(k/k_1)^n + P_{\text{SN}}$ , where  $k_1 = 0.1 \text{ arcmin}^{-1}$ . We also make use of the halo model approach to model-fit our clustering measurements, making use of the halo occupation distribution (HOD)<sup>41</sup>.

The number of pairs of galaxies inside a given halo depends on the variance of the HOD,  $\sigma^2(M, z) = \langle N_{\text{gal}}(N_{\text{gal}} - 1) \rangle$  while the number of pairs of galaxies in different halos is simply given by the square of the mean halo occupation with  $N(M, z) = \langle N_{\text{gal}} \rangle$ , where  $N_{\text{gal}}$  is the total number of galaxies in a halo and we further assume that one galaxy occupies the center of the halo, the others being considered as satellite galaxies, so that  $N_{\text{gal}} = N_{\text{cen}} + N_{\text{sat}}$ . Central and satellite galaxies are assumed to have different HODs; in fact the mean number of central galaxies in a given halo is a simple step function, so that  $N_{\text{cen}} = 1$  above a given mass  $M_{\text{min}}$ , and  $N_{\text{cen}} = 0$  otherwise. The HOD of satellite galaxies is taken to be a power law of the halo mass<sup>42</sup>:

$$N_{\text{sat}} = \left( \frac{M}{M_1} \right)^\alpha ; \quad (8)$$

here  $M_1$  is a normalization factor that represents the mass scale at which a single halo hosts on average one satellite galaxy in addition to the central galaxy.

The power spectrum of galaxies is then parameterized as the sum of two different contributions: the 1-halo term, which describes the clustering on small scales and is related to pairs of galaxies within the same halo and the 2-halo term, responsible for the large scale clustering and related to pairs of galaxies in different halos:

$$P(k, z) = P_{1\text{h}}(k, z) + P_{2\text{h}}(k, z). \quad (9)$$

The two terms are then written as:

$$\begin{aligned} P_{1\text{h}}(k, z) &= \int dM \frac{dn_{\text{halo}}}{dM}(z) [2N_{\text{cen}}(M)N_{\text{sat}}(M)u_{\text{DM}}(k, z|M) + \\ &\quad N_{\text{sat}}^2(M)u_{\text{DM}}^2(k, z|M)] dM / n_{\text{gal}}^2(z), \\ P_{2\text{h}}(k, z) &= P_{\text{DM}}(k, z) \times \\ &\quad \left[ \int dM \frac{dn_{\text{halo}}}{dM}(z) N_{\text{gal}}(M, z) \times \right. \\ &\quad \left. b(M, z)u_{\text{DM}}(k, z|M) dM \right]^2 / n_{\text{gal}}^2(z). \end{aligned} \quad (10)$$

Here  $P_{\text{DM}}(k, z)$  is the linear dark matter power spectrum;  $n_{\text{halo}}$  is the halo-mass function<sup>43</sup>;  $b(M, z)$  is the linear bias which connects the large scale clustering of dark matter to the galaxy clustering;  $u_{\text{DM}}(k, z|M)$  is the normalized dark matter halo density profile in Fourier space (as a function of wavenumber  $k$  and redshift  $z$  for a given value of mass  $M$ ) and  $n_{\text{gal}}$  is the mean number of galaxies per unit comoving volume at redshift  $z$ :

$$n_{\text{gal}}(z) = \int dM \frac{dn_{\text{halo}}}{dM}(z) \left[ 1 + \left( \frac{M}{M_1} \right)^\alpha \right]. \quad (11)$$

For the dark matter halo density function we adopt the Navarro-Frenk-White<sup>44</sup> profile truncated at the virial radius  $r_{\text{vir}}$  and with a concentration parameter given by:

$$c(M, z) = \frac{9}{1+z} \left( \frac{M}{M_*} \right)^{-0.13}; \quad (12)$$

here  $M_*$  is the characteristic mass scale at which the critical density required for spherical collapse is equal to the square root of the variance in the initial density field  $\sigma(M)$  when extrapolated at the present time using linear theory such that  $\delta_{\text{sc}}(z) = \sigma(M_*)$ , where  $\delta_{\text{sc}}(z) = 1.68/g(z)$ , where  $g(z)$  is the linear theory growth function for density perturbations.

As outlined above  $M_{\text{min}}$  determines both the one-halo and two-halo amplitudes, while  $\alpha$  determines primarily the amplitude of the one-halo term and the overall number density of galaxies, which in return is connected to the amplitude of the two halo term via the halo bias factor. While with the two-halo term alone all these parameters are degenerate with each other and the bias factor, allowing only an average mass scale to be determined based on the bias factor, with one-halo term also included some of the degeneracies are broken and  $M_{\text{min}}$  and  $\alpha$  can be determined independent of bias<sup>12</sup>.

In the Limber approximation, the measured power spectrum of fluctuations can be expressed as the 2 dimensional, flux averaged projection of the three-dimensional galaxy power spectrum  $P(k, z)$  as:

$$P(k_\theta) = \int_{z_{\text{min}}}^{z_{\text{max}}} P \left( k = \frac{2\pi k_\theta}{x(z)}, z \right) \left( \frac{dS}{dz}(z) \right)^2 \frac{1}{dV_c(z)} dz; \quad (13)$$

here  $dS/dz$  is the redshift distribution of the cumulative flux contributed by the background faint galaxies,  $dV_c$  is the comoving volume element, defined as  $dV_c \equiv x(z)^2 \frac{dx}{dz}$  and  $x(z)$  is the comoving radial distance.

In this paper we determine the redshift distribution of the intensity by binning the redshift range in four redshift bins between  $z = 0$  and  $z = 4$  and putting constraints on  $dS/dz$  in each bin; the advantage of this approach is that we don't assume a particular model for  $dS/dz(z)$ ; instead, we let the data decide which model is more adequate.

The method we use to constrain our parameters is based on a modified version of the publicly available Markov-Chain Monte-Carlo (MCMC) package CosmoMC<sup>45</sup>, with a convergence diagnostics based on the Gelman-Rubin criterion<sup>46</sup>. We consider a halo model described by the following set of parameters:

$$\{dS/dz_i, M_{\text{min}}, \alpha, M_1, P_{\text{SN}}\}, \quad (14)$$

where, as discussed before, we bin the cumulative flux  $dS/dz(z)$  in four redshift bins,  $dS/dz_i(z)$  ( $i = 1, 2, \dots, 4$ ), representing the value at four redshift intervals,  $\text{bin}_i \in [0 - 1, 1 - 2, 2 - 3, 3 - 4]$ . In the above  $P_{\text{SN}}$  is the shot-noise amplitude which we remeasure again for the halo model fits. To obtain

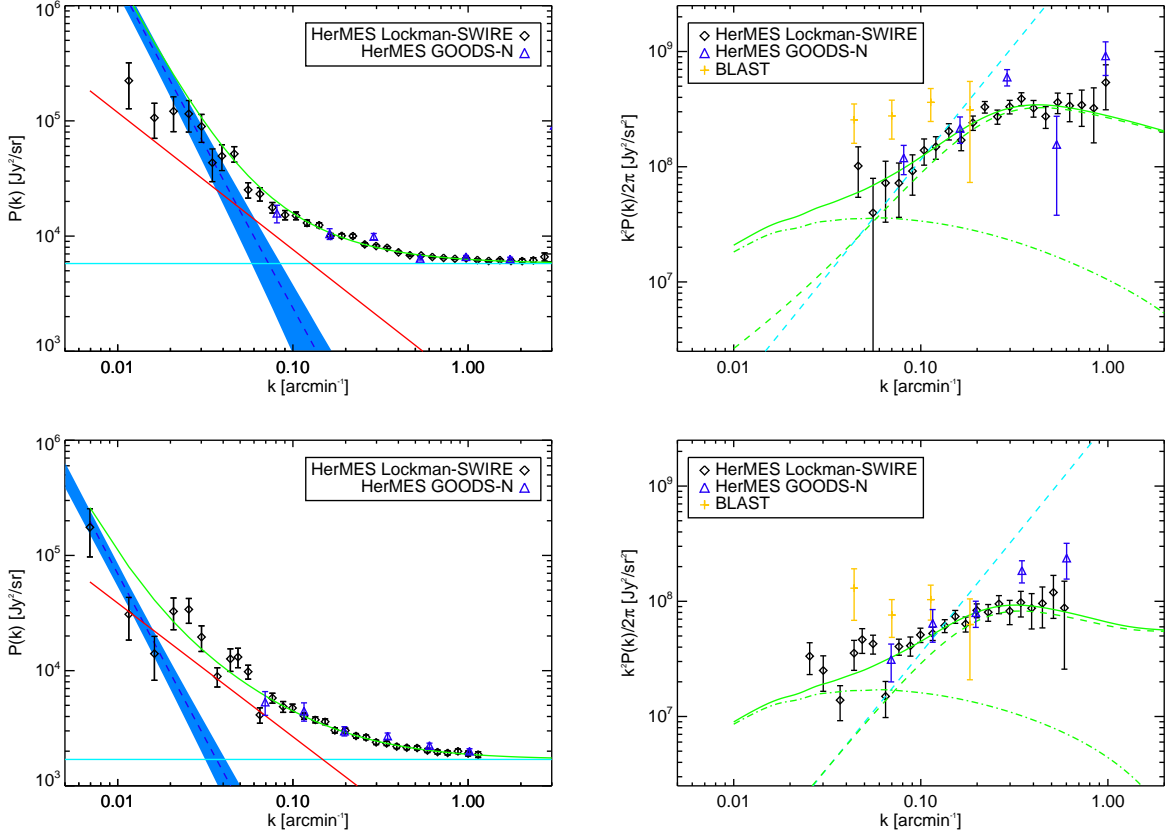


Figure S 10: **The fluctuation power spectrum and the clustering component.** The total power spectrum  $P(k)$  (left panels) and clustering  $P(k)$  with shot-noise removed (right panels) at  $250 \mu\text{m}$  (top) and  $500 \mu\text{m}$  (bottom), respectively. The power spectrum measurements shown are binned logarithmically for  $k > 0.03 \text{ arcmin}^{-1}$ , with a bin width equal to  $\Delta k/k = 0.15$ , and linearly for smaller  $k$ , with a bin width of  $\Delta k = 4.6 \times 10^{-3} \text{ arcmin}^{-1}$ . This figure is similar to Fig 1.

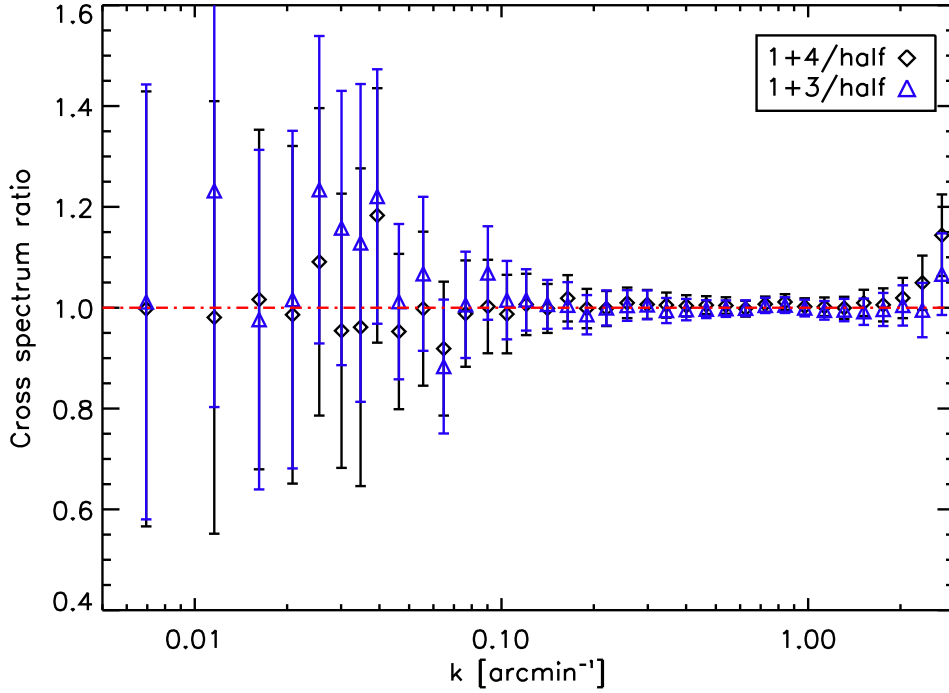


Figure S 11: **Accuracy of the power spectrum measurement.** Ratios of the total power spectra  $P(k)$  estimated with different sub-maps of Lockman-SWIRE data normalized to the default power spectrum shown in the main paper estimated with the  $(1 + 2)$  map cross-correlated against the  $(3 + 4)$  map, after the data are divided into four sequential intervals in time, labeled 1 to 4, of equal duration. The 1 and 3 subsets have the same scan direction and the 2 and 4 subsets have the same scan directions, but the two subsets are almost orthogonal.

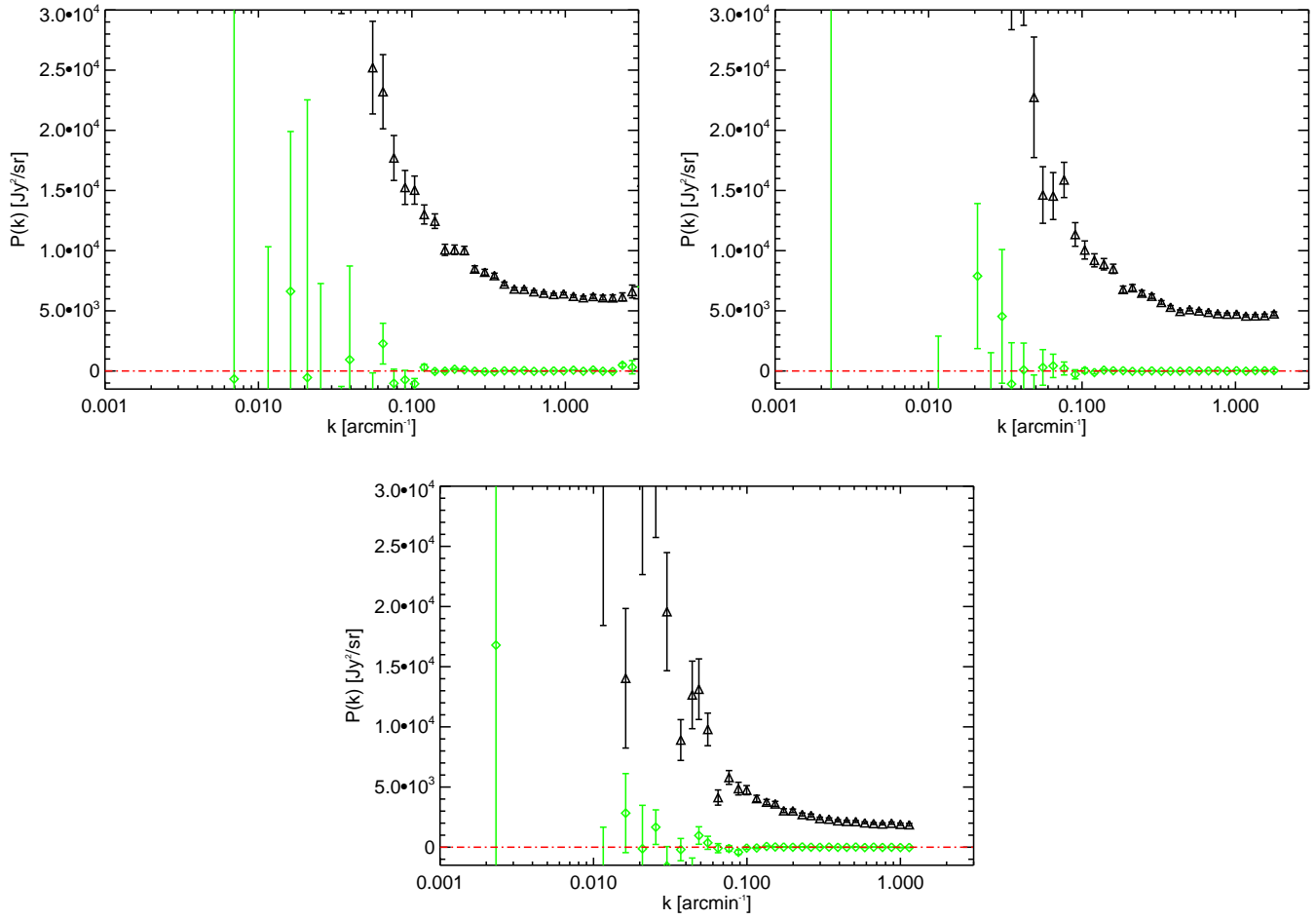


Figure S 12: **The null-test of the power spectrum measurement.**  $P(k)$  measured (black triangle) on Lockman-SWIRE with the cross spectrum  $[(1 + 2) \times (3 + 4)]$  at 250, 350, 500  $\mu\text{m}$  (left to right, top to bottom). Cross power spectrum (green diamond) of the difference  $[(1 - 2) \times (3 - 4)]$ .

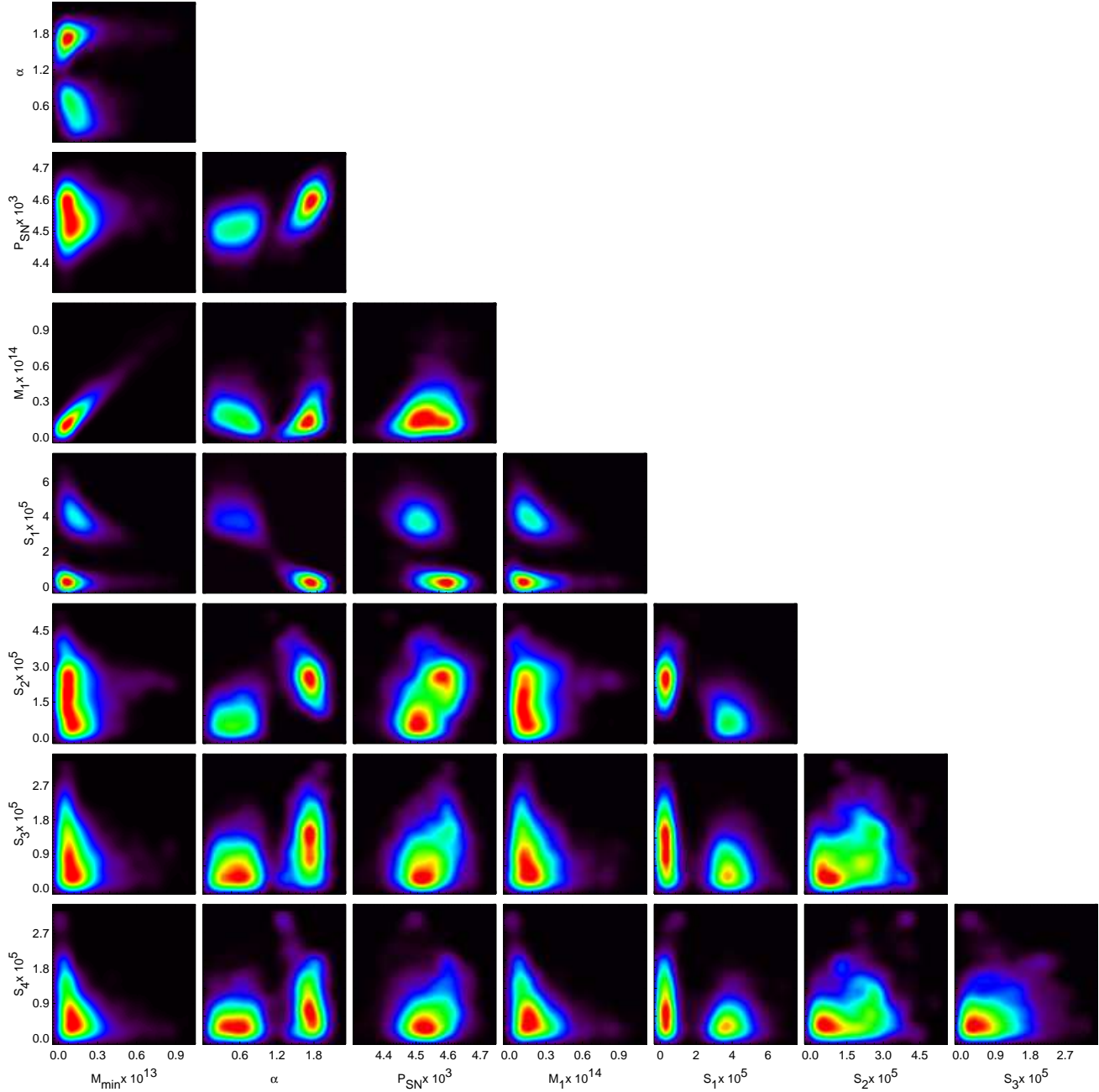


Figure S 13: **The halo model parameter estimates.** Bi-dimensional probability distribution function for all the pairs associated with our halo model fits with eight parameters ( $M_1$ ,  $M_{min}$ ,  $\alpha$ ,  $P_{SN}$ ,  $S_1$ ,  $S_2$ ,  $S_3$  and  $S_4$ ) showing our constraints and the degeneracies between the parameters. Here we show results at  $350 \mu\text{m}$ , but degeneracies of parameters related to  $250$  and  $500 \mu\text{m}$  model fits are similar.

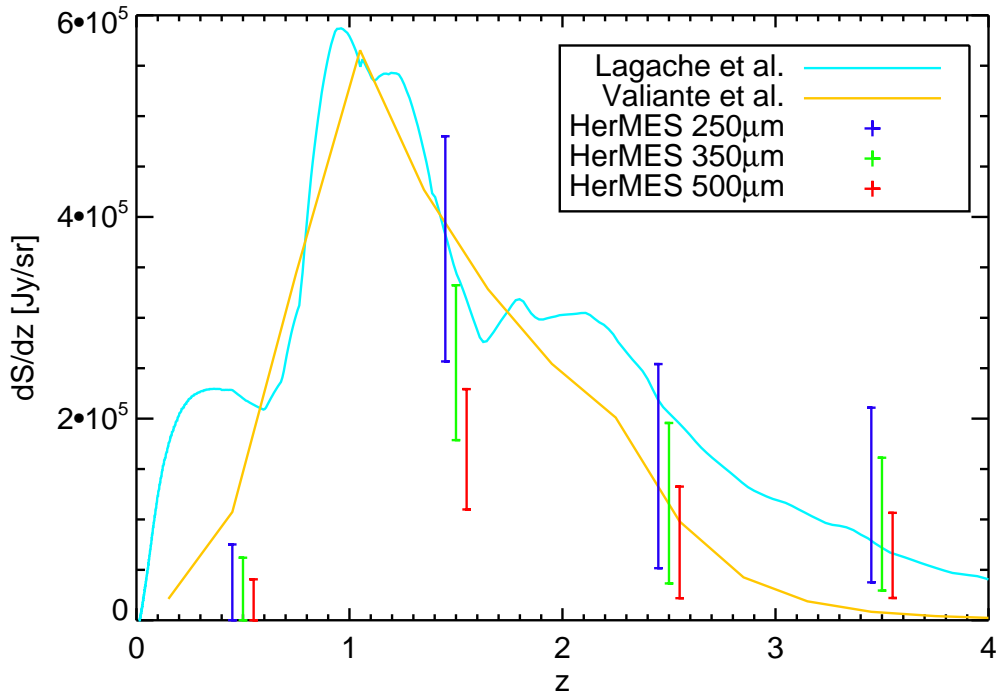


Figure S 14: **Redshift evolution of the galaxy intensities at the sub-millimetre wavelengths.**  $dS/dz$  as a function of redshift for 4 bins in redshift and for the three wavebands of SPIRE with  $S < 50$  mJy. For reference, we show 2 model predictions from Lagache et al.<sup>37</sup> and Valiante et al.<sup>38</sup> for the same flux cut. We have used a prior on the occupation number slope  $\alpha > 1$ .

reliable model-fits to data we set a broad uniform prior on the ratio  $M_1/M_{\min}$  to be between 10 to 25, consistent with numerical simulations of the halo occupation distribution which finds a value close to 15 for this ratio<sup>47</sup>. We also require that the redshift integrated source intensity be within the 68% confidence level ranges of the background light intensities as obtained by FIRAS<sup>48</sup>. The central values and errors we use are  $0.85 \pm 0.08$ ,  $0.65 \pm 0.19$  and  $0.39 \pm 0.10$  MJy/sr at 250, 350, and 500  $\mu\text{m}$ , respectively. For background cosmology, we assume the concordance model<sup>49</sup>. Our results related to the halo model fits are summarized in Table S2.

In comparison to the shot-noise values from model fits to the power spectrum (Table S1 for the power-law case and Table S2 for the halo model case), the shot-noise values from the best determined source counts<sup>50</sup> give  $6900 \pm 320$ ,  $4500 \pm 220$ , and  $1600 \pm 100$  Jy<sup>2</sup>/sr at 250, 350, and 500  $\mu\text{m}$ , respectively.

In Figure S13 we show the two-dimensional constraints on pairs of parameters that highlight the degeneracies associated with this eight parameter model fit. The best-fit values and the errors at each of the three wavebands are show in Figure S14.

Additionally, we compute the far-infrared bolometric luminosity between 8 and 1100  $\mu\text{m}$  in each of the redshift bins from the  $dS/dz(z)$  values by modelling the flux received between a redshift  $z_{\min}^i$  and  $z_{\max}^i$  in each  $j$  SPIRE bands, defined by the bandpass  $f_j(\nu)$ :

$$dS^j/dz^i = L_{\text{FIR}} \int_{z_{\min}^i}^{z_{\max}^i} dz \frac{(1+z)^{(\beta+1)}}{4\pi D_L^2(z)} \frac{\int_{270 \text{ GHz}}^{38 \text{ THz}} \nu^\beta B(\nu(1+z), T) f_j(\nu) d\nu}{\int_{270 \text{ GHz}}^{38 \text{ THz}} \nu^\beta B(\nu, T) d\nu} \quad (15)$$

The temperature  $T$  is chosen to be  $28 \pm 8$  K and the emissivity index  $\beta$  is fixed to 1.5, we then fit for  $L_{\text{FIR}}$  given the measured values and the predicted values of  $dS/dz_i$ . The temperature uncertainty is incorporated into the  $L_{\text{FIR}}$  error budget. We summarize our results related to  $L_{\text{FIR}}$  as a function of redshift in Figure 2.  $L_{\text{FIR}}$  is a measure of the star-formation rate with<sup>51</sup>

$$\text{SFR}[\text{M}_\odot \text{yr}^{-1}] = 1.73 \times 10^{-10} L[\text{L}_\odot]. \quad (16)$$

We use this to also show the SFR implied by  $L_{\text{FIR}}$  in Figure 2. Here we have subselected the models that lead to  $\alpha > 1$  to be consistent with the occupation numbers at other wavelenegths<sup>41,42</sup>.  $L_{\text{FIR}}$  as a function of redshift has been predicted in two analytical models of sub-millimetre galaxy population<sup>37,38</sup> and we make a comparison in the same figure.

## References:

31. Ott, S. 2010, in *Astronomical Data Analysis Software and Systems XIX*, ed. Y.Mizumoto, K.-I. Morita, and M. Ohishi, ASP Conf. Series.
32. Levenson, L. et al. 2010, *Mon. Not. R. Astron. Soc.* in press, arXiv.org:1010.0020
33. Swinyard, B. et al. In-flight calibration of the Herschel-SPIRE instrument, *Astron. Astrophys.* 518, L4 (2010).
34. Fixsen, D.J., Moseley, S.H. & Arendt, R.G. Calibrating Array Detectors, *Astrophys. J. Supp.* 128, 651-658 (2000).
35. Hivon, E. et al. MASTER of the Cosmic Microwave Background Anisotropy Power Spectrum: A Fast Method for Statistical Analysis of Large and Complex Cosmic Microwave Background Data Sets. *Astrophys. J.* 567, 2-17 (2002).
36. Knox, L., *Phys. Rev. D.*, 52, 4307-4318 (2005).
37. Lagache, G., Dole, H. & Puget, J.-L. Modelling the infrared galaxy evolution using a phenomenological approach, *Mon. Not. R. Astron. Soc.* 338, 555-571 (2003).
38. Valiante, E. et al. A Backward Evolution Model for Infrared Surveys: The Role of AGN- and Color- $L_{\text{TIR}}$  Distributions. *Astrophys. J.* 701, 1814-1838 (2009).

39. Lagache, G. Bavouzet, N., Fernandez-Conde, N. et al. Correlated Anisotropies in the Cosmic Far-Infrared Background Detected by the Multiband Imaging Photometer for Spitzer: Constraint on the Bias. *Astrophys. J.* 665, L89-L92 (2007).
40. Schlegel, D. J., Finkbeiner, D. P., Davis, M. Maps of Dust Infrared Emission for Use in Estimation of Reddening and Cosmic Microwave Background Radiation Foregrounds. *Astrophys. J.* 500, 525-534 (1998).
41. Cooray, A., Sheth, R. Halo models of large scale structure. *Phys. Rep.* 372, 1-129 (2002).
42. Zehavi I., et al. *Astrophys. J.*, 630, 1-27 (2005).
43. Sheth, R. K., Mo, H. J., Tormen, G. Ellipsoidal collapse and an improved model for the number and spatial distribution of dark matter haloes. *Mon. Not. Roy. Astron. Soc.* 323, 1-12 (2001).
44. Navarro, J. F., Frenk, C. S., White, S. D. M. A Universal Density Profile from Hierarchical Clustering. *Astrophys. J.* 490, 493-510 (1997).
45. Lewis, A. & Bridle, S. Cosmological parameters from CMB and other data: A Monte Carlo approach. *Phys. Rev. D.* 66, 103511 (2002).
46. Gelman, A., Rubin, D. B. Inference from iterative simulation using multiple sequences. *Statistical Science.* 7, 457-472 (1992).
47. Zheng, Z. et al. Theoretical Models of the Halo Occupation Distribution: Separating Central and Satellite Galaxies, *ApJ*, 633, 791-809 (2005).
48. Fixsen, D. J., Dwek, E., Mather, J. C., Bennett, C. L. & Shafer, R. A. The spectrum of the extragalactic far-infrared background from the COBE FIRAS observations. *Astrophys. J.* 508, 123-128 (1998).
49. E. Komatsu et al. Seven-Year Wilkinson Microwave Anisotropy Probe (WMAP) Observations: Cosmological Interpretation, *Astrophys. J. Supp.* submitted, arXiv.org:1001.4538 (2010).
50. Glenn, J. et al. HerMES: Deep Galaxy Number Counts from a P(D) Fluctuation Analysis of SPIRE Science Demonstration Phase Observations, *Mon. Not. R. Astron. Soc.* in press, arXiv.org:1009.5675 (2010).
51. Kennicutt, R. C. Jr. Star Formation in Galaxies Along the Hubble Sequence, *Ann. Rev. of Astron. Astrophys.* 36, 189-232 (1998).